

<https://helda.helsinki.fi>

A Possible Link between Turbulence and Plasma Heating

Yordanova, Emiliya

2021-11

Yordanova , E , Voros , Z , Sorriso-Valvo , L , Dimmock , A P & Kilpua , E 2021 , ' A Possible Link between Turbulence and Plasma Heating ' , Astrophysical Journal , vol. 921 , no. 1 , 65 . <https://doi.org/10.3847/1538-4357/ac1942>

<http://hdl.handle.net/10138/345407>

<https://doi.org/10.3847/1538-4357/ac1942>

cc_by

publishedVersion

Downloaded from Helda, University of Helsinki institutional repository.

This is an electronic reprint of the original article.

This reprint may differ from the original in pagination and typographic detail.

Please cite the original version.



A Possible Link between Turbulence and Plasma Heating

Emiliya Yordanova¹ , Zoltán Vörös^{2,3} , Luca Sorriso-Valvo^{1,4} , Andrew P. Dimmock¹ , and Emilia Kilpua⁵

¹ Swedish Institute of Space Physics, Uppsala, Sweden; eya@irfu.se

² Space Research Institute, Austrian Academy of Sciences, Graz, Austria

³ Institute of Earth Physics and Space Science, Eötvös Loránd Research Network, Sopron, Hungary

⁴ CNR—Istituto per la Scienza e Tecnologia dei Plasmi, Bari, Italy

⁵ Department of Physics, University of Helsinki, Helsinki, Finland

Received 2021 March 19; revised 2021 July 26; accepted 2021 July 28; published 2021 November 1

Abstract

Numerical simulations and experimental results have shown that the formation of current sheets in space plasmas can be associated with enhanced vorticity. Also, in simulations the generation of such structures is associated with strong plasma heating. Here, we compare four-point measurements in the terrestrial magnetosheath turbulence from the Magnetospheric Multiscale mission of the flow vorticity and the magnetic field curlometer versus their corresponding one-point proxies PVI(V) and PVI(B) based on the Partial Variance of Increments (PVI) method. We show that the one-point proxies are sufficiently precise in identifying not only the generic features of the current sheets and vortices statistically, but also their appearance in groups associated with plasma heating. The method has been further applied to the region of the turbulent sheath of an interplanetary coronal mass ejection (ICME) observed at L1 by the WIND spacecraft. We observe current sheets and vorticity associated heating in larger groups (blobs), which so far have not been considered in the literature on turbulent data analysis. The blobs represent extended spatial regions of activity with enhanced regional correlations between the occurrence of conditioned currents and vorticity, which at the same time are also correlated with enhanced temperatures. This heating mechanism is substantially different from the plasma heating in the vicinity of the ICME shock, where plasma beta is strongly fluctuating and there is no vorticity. The proposed method describes a new pathway for linking the plasma heating and plasma turbulence, and it is relevant to in situ observations when only single spacecraft measurements are available.

Unified Astronomy Thesaurus concepts: [Plasma physics \(2089\)](#); [Interplanetary turbulence \(830\)](#); [Solar coronal mass ejections \(310\)](#)

1. Introduction

Heating in astrophysical plasmas in the absence of collisions still remains an unsolved question. The first spacecraft missions have already revealed that the solar corona is much hotter than the solar surface. Even more remarkably, the solar wind during its expansion does not cool adiabatically, implying that local mechanisms are continuing to heat the particles in the interplanetary (IP) space. Although MHD models of turbulence transport can predict, for example, the profiles of fluctuating kinetic energy, density, and proton temperature with heliocentric distance, the turbulent model heating depends on parameterization and phenomenological assumptions without the direct incorporation of the local microphysics of kinetic energy dissipation (Zank et al. 2017; Adhikari et al. 2019). To understand local heating mechanisms in collisionless plasmas the corresponding kinetic plasma processes have to be understood. To date, there are several decades of in situ spacecraft observations of the solar wind in the heliosphere and detailed measurements in the near-Earth plasma regions that have evidenced one or another physical mechanism of collisionless plasma heating. These include—to name a few—linear wave damping, stochastic heating (Chandran et al. 2010), magnetic reconnection, microinstabilities (Gary 2015, and references therein), and plasma turbulence (and references therein Chen et al. 2019). However, their relative contribution and importance are still largely unknown. Reconnecting, turbulence-generated small-scale (sub-ion scale) current sheets are also considered a possible physical mechanism associated with small-scale energy conversion and dissipation. Recent simulations have shown that the intermittently occurring current sheets in turbulence are

accompanied by other coherent structures, such as vortices, density structures, gradients of different quantities (Matthaeus 2021), and at the kinetic level, by distortions of the pressure tensor (Del Sarto et al. 2016). These coherent structures are not overlapping, but spatially separated over distances comparable to ion inertial length (d_i). Recent analysis based on both fluid and kinetic scale plasma simulations and by using multispecies Vlasov–Maxwell formulations suggest that the physical quantities associated with multi-scale energy transfer and energy conversions show the same type of intermittent and localized spatial concentrations nearby the coherent structures and gradients (Matthaeus et al. 2020). This indicates that there might exist several channels of energy conversion/dissipation and plasma heating associated with spatially concentrated small-scale coherent structures (Matthaeus 2021). There is an ongoing debate as to whether the plasma heating is concentrated at thin current sheets (with a thickness of the order d_i) (Valentini et al. 2016; Pezzi et al. 2018), nearby the current sheets at plasma vortices (Jain et al. 2017), or at locations of enhanced pressure–strain interactions (Chasapis et al. 2018b). The latter is associated with the energy conversion between flow and random particle motions; therefore, in fully kinetic simulations the pressure–strain work was found to be correlated with velocity gradients (Yang et al. 2017). Although there are no local pointwise correlations between the coherent structures and physical quantities associated with energy transfer and conversion, these are colocated within regions of size comparable to d_i . Therefore, some coarse-grained or regional correlations can be expected between them (Yang et al. 2019). The generation of intermittent small-scale coherent structures is

theoretically not fully understood. It might be the consequence of self-organization processes operating as the turbulent cascade is transferring energy from large scales toward the kinetic scales (Matthaeus et al. 2015). Similarly, the explanation of the occurrence of magnetically dominated meso-scale structures, such as flux ropes, magnetic islands, their interactions, and relation to the turbulent energy transfer rate represent further theoretical challenges. Nevertheless, in the solar wind, magnetic islands and current sheets represent the basic ingredients in explaining plasma heating and particle acceleration. Small-scale islands can also result from magnetic reconnection within the heliospheric current sheet (HCS; Zhao et al. 2020) or various interactions between large-scale structures, such as the HCS and stream interfaces (Adhikari et al. 2020), and the HCS and the heliospheric termination shock (Zhao et al. 2019). Local acceleration observed at 5 au was attributed to the interaction of such magnetic islands (Zhao et al. 2018).

In this work, we focus specifically on the heating in turbulent plasmas that is associated with the generation of specific structures by turbulence. Observations in the solar wind have revealed that current layers arising from turbulence develop complex sub-proton networks of secondary islands and very thin current sheets in the regions of reconnection outflows (Greco et al. 2016). In simulations, these thin current sheets have been associated with strong electron heating (Hesse et al. 2001). We aim to use proxies for vorticity and current sheets that can be calculated from one-point measurements in the solar wind, where the time resolution of field and plasma measurements is also limited. As a consequence, the identification of thin ion/electron-scale structures potentially associated with plasma heating might not be resolved. Our working hypothesis is that due to turbulent intermittency, heating can happen in larger-scale blobs, which are presumably much larger than the ion inertial length. In fact, the meaning of turbulent intermittency is that the turbulent energy is spatially non-homogeneous, i.e., there are voids in space with less kinetic energy and volumes where the energy is concentrated. In those blobs, the occurrence of vortical flows that might potentially generate current sheets is presumably also enhanced. In such *active* blobs there might exist an *integrated* elevated temperature, relative to the ambient plasma, which could be observed more easily than the heating signatures at localized ion/electron-scale structures. Also, the limited time resolution of single spacecraft in the solar wind would be less restrictive for the identification of larger-scale active blobs. However, the usefulness of one-point proxies has to be tested. To this end, we use multipoint measurement techniques for physical quantities such as vorticity and current density from the Magnetospheric Multiscale (MMS) mission. This allows us to test the four-point high time resolution estimation of vorticity $|\nabla \times \mathbf{V}|$ and curlometer $|\nabla \times \mathbf{B}|$ versus one-point proxies $\text{PVI}(V)$ and $\text{PVI}(B)$ with smaller temporal resolution. Although we do not expect one-to-one correspondence, the proxies should allow us to correlate the turbulence-generated intermittent structures with intermittent heating in the solar wind. In order to test the proxies on high quality estimators of $|\nabla \times \mathbf{V}|$ and $|\nabla \times \mathbf{B}|$, we have selected intervals of MMS observations in the turbulent terrestrial magnetosheath (MSH). After showing that the proxies work in the MSH we apply the same approach to the turbulent sheath region of an interplanetary coronal mass ejection (ICME). This way we attempt to understand the integrated role of groups of thin current sheets and the associated vorticity in active intermittent blobs to global plasma heating rather than the heating at individual current sheets.

2. Observations and Method

For the analysis in this study, we use in situ data from the multipoint MMS mission and the solar wind monitor WIND, positioned at L1. The MMS observations were performed on the dayside terrestrial MSH proper and the flanks (shown in Figure 1), while the WIND measurements originate from an event of relatively fast ICME.

2.1. MMS Observations

The four MMS spacecraft are equipped with the same state-of-the-art suite of instruments providing unprecedented high temporal and spatial resolution plasma and electromagnetic field measurements (Burch et al. 2016). The spacecraft form a tetrahedron configuration at very close separation (approximately tens of kilometers). The main scientific objective of the mission is to resolve magnetic reconnection and kinetic scales plasma processes. We use magnetic field data measured by the Fluxgate Magnetometer instrument (Russell et al. 2014) at a sampling frequency of 128 Hz; and electron and ion moments from the Fast Plasma Investigation instrument (Pollock et al. 2016) at sampling rates of 150 and 30 ms, respectively.

Two separate time intervals of MMS multipoint observations are considered. The first time interval consists of MMS observations of the turbulent MSH on 2015 November 30 between 00:21 and 00:26 UTC. During this time the MSH was downstream of a quasi-parallel bow shock (Figure 1, left panels). Thanks to the recent multipoint Cluster (Escoubet et al. 2001) and MMS missions, it has been well established that the MSH under this geometry is characterized by strong and intensive fluctuations and it is very dynamic (Echim et al. 2021, and references therein). Observations also indicate that under such turbulent conditions current sheets of the characteristic scale of the ion inertial length are present at high rates of occurrence (Vörös et al. 2016; Yordanova et al. 2020). At turbulent current sheets various kinetic processes take place, such as plasma heating (Chasapis et al. 2015, 2017, 2018a), plasma acceleration (Eriksson et al. 2016a), magnetic reconnection (Phan et al. 2007, 2018; Retinò et al. 2007; Yordanova et al. 2016; Vörös et al. 2017), and turbulent dissipation (Sundqvist et al. 2007; Vörös et al. 2019b).

The second interval is an observation of Kelvin–Helmholtz (KH) vortices at the duskside magnetopause on 2015 September 8, between 10:07 and 11:25 UTC (Figure 1, right panels). This period has been studied previously in terms of spectral and scaling properties of turbulence (Stawarz et al. 2016; Quijia et al. 2021). In another study (Sorriso-Valvo et al. 2019) in the same KH interval, a strong connection was found between the local turbulent energy transfer at the end of inertial range and the development of non-Maxwellian features of the ion velocity distribution functions (VDFs), such as parallel ion beams. In addition, plasma jets at reconnecting current sheets were reported in the same event (Eriksson et al. 2016b).

2.2. WIND Observations

We also use in situ measurements from L1 from the WIND spacecraft during an ICME passage on 2013 March 17–18. This ICME was associated with a significant solar energetic particle event and triggered a strong geomagnetic storm (Wu et al. 2016). We analyze 3 s solar wind proton data from the WIND 3D Plasma and Energetic Particle Investigation instrument (Lin et al. 1995), and 0.092 s magnetic field

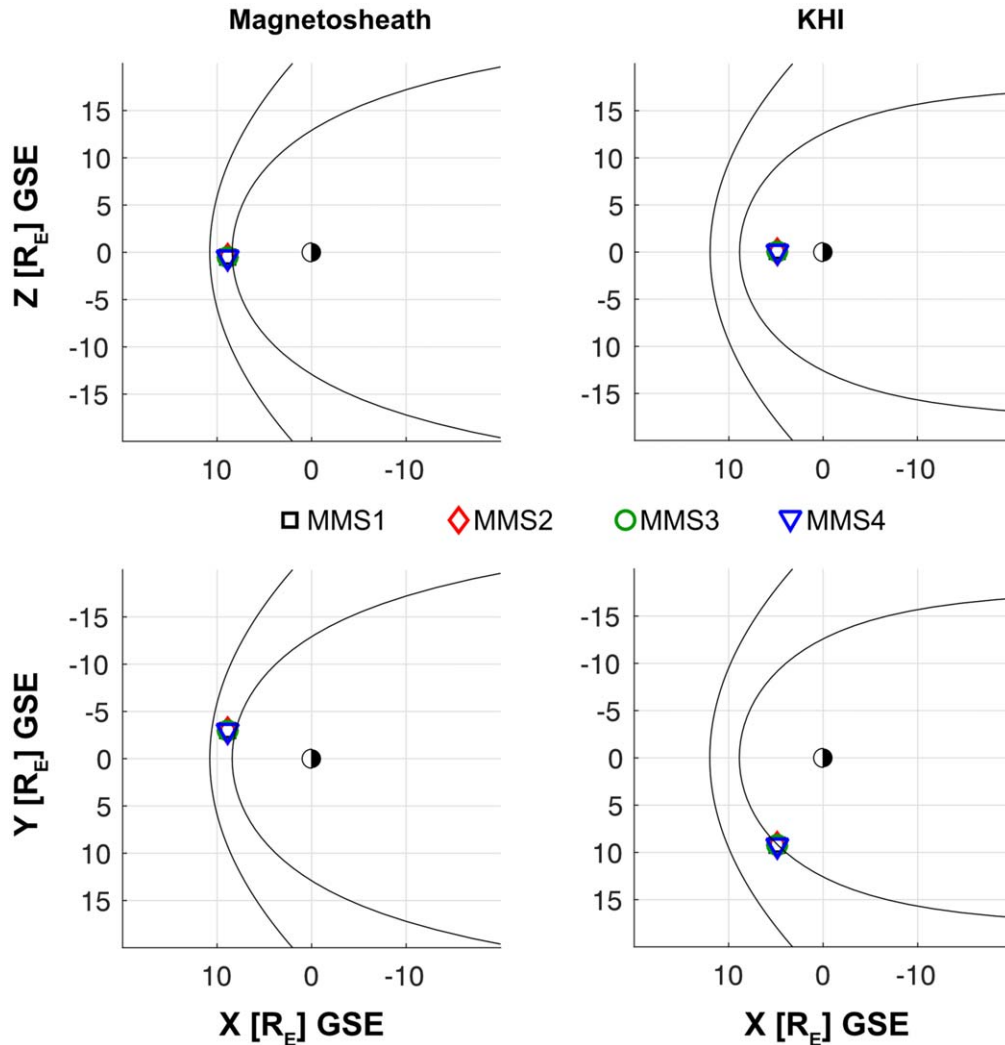


Figure 1. MMS position in the XZ and XY planes in the Geocentric Solar Ecliptic (GSE) frame during the MSH (left) and during the Kelvin–Helmholtz instability (KHI) intervals (right). The inner parabolic curve represents the modeled magnetopause and the outer one—the bow shock using 1 h upstream data from the OMNI database. Note that MMS separation is much smaller than the Earth radius R_E , therefore, the spacecraft symbols are overlapping.

observations from the Magnetic Field Investigation instrument (Lepping et al. 1995). We take particular interest in the sheath region of the ICME. The ICME sheaths are formed when a CME ejecta propagates sufficiently faster than the ambient IP plasma (Kilpua et al. 2017, 2019), producing a shock wave, behind which the solar wind plasma is collected and compressed by the expanding CME. Recent studies of the ICME sheaths (Kilpua et al. 2020, 2021) show that they are turbulent regions, with fluctuations amplitude, compressibility, and intermittency levels higher than that of the background solar wind.

Even though the three cases considered here, namely, a turbulent MSH, a duskside magnetopause KH interval, and an ICME sheath, may seemingly represent different plasma regions, they share in common a high level of turbulence, and the plasma is compressed and bounded by boundaries. The velocity shear at the magnetopause leads to a growth of KHI rolling-in layers of plasma with MSH and magnetospheric origin in vortices. In the MSH, the plasma is confined between the bow shock and the magnetopause, while the ICME sheath is confined by the IP shock and the leading edge of the ICME magnetic ejecta. It is worth noting, however, that the MSH and

ICME sheath have different origins (Siscoe & Odstrcil 2008). The former is of a *propagation* type of a sheath layer, where the incoming solar wind flows sideways the obstacle (Earth) from the nose of the bow shock, while the latter is in general a combination of a *propagation* and *expansion* type. As the CME expands, the flow is deflected around it but at much slower speed resulting in a plasma pile-up instead of lateral flows around.

2.3. Methods

The Partial Variance of Increments (PVI) method has been broadly used in the analysis of turbulent plasmas (Greco et al. 2009; Matthaeus et al. 2015; Greco et al. 2018, and references therein; Kilpua et al. 2020; Yordanova et al. 2020) since its first application in MHD simulations (Greco et al. 2008; Servidio et al. 2011). The PVI is a tool for identification of discontinuities in the magnetic field and plasma parameters. In single-point observations, the PVI is calculated by estimating the magnetic field increments, that is, the magnitude of the vectorial differences $\Delta Q(t, \tau) = Q(t) - Q(t + \tau)$ of a quantity Q , which is then normalized

by the square root of their variance:

$$\text{PVI}(t, \tau) = \sqrt{\frac{|\Delta \mathbf{Q}(t, \tau)|^2}{\langle |\Delta \mathbf{Q}(t, \tau)|^2 \rangle}}, \quad (1)$$

where the averaging is done over the entire data sample and τ is the time delay between two instances of measurement, which defines the scale of the fluctuations of interest. Assuming the validity of the Taylor hypothesis (Taylor 1938), which supposes that the inherent plasma structures do not evolve in time or evolve much slower than the plasma flows past the spacecraft, the temporal scales can be transformed into spatial scales. The PVI can be calculated from a vector field, e.g., velocity or magnetic field, or a scalar, such as plasma density. The availability of multipoint Cluster and MMS measurements allowed for the method to be adapted and applied to two-point measurements from pairs of spacecraft (Chasapis et al. 2015; Vörös et al. 2016; Yordanova et al. 2016). In that case, Equation (1), is rewritten as

$$\text{PVI}_{ij}(t) = \sqrt{\frac{|\Delta \mathbf{Q}_{ij}(t)|^2}{\langle |\Delta \mathbf{Q}_{ij}(t)|^2 \rangle}}, \quad (2)$$

where again the average $\langle \cdot \rangle$ is taken over the whole data interval, and $i, j = 1, 2, 3,$ and 4 refers to the spacecraft number. The increments $\Delta \mathbf{Q}_{ij}(t) = \mathbf{Q}_i(t) - \mathbf{Q}_j(t)$ are now estimated between two points of measurement (i.e., pairs of spacecraft), thus, they represent the typical fluctuations over the actual spatial distance between the spacecraft. This means that PVI from multipoint measurements is sensitive to structures with sizes comparable to the distance between spacecraft.

In similar fashion, one can calculate the rotation or shear angles in a given vector field, from single-point measurements:

$$\alpha(t, \tau) = \cos^{-1} \frac{\mathbf{Q}(t) \cdot \mathbf{Q}(t, \tau)}{|\mathbf{Q}(t)| \cdot |\mathbf{Q}(t, \tau)|}, \quad (3)$$

and from multipoint measurements:

$$\alpha_{ij}(t) = \cos^{-1} \frac{\mathbf{Q}_i(t) \cdot \mathbf{Q}_j(t)}{|\mathbf{Q}_i(t)| \cdot |\mathbf{Q}_j(t)|}. \quad (4)$$

The calculation of the shear angle is useful in complementing the PVI method to distinguish between discontinuities ($\text{PVI} > 3$) with or without large rotations, indicating the presence or absence of current sheets (Chasapis et al. 2015).

An additional advantage of multipoint measurements is the estimation of the spatial gradient tensors across the tetrahedron configuration of spacecraft. We can calculate the gradient tensor of the magnetic field and the vorticity of the velocity field as $\nabla \times \mathbf{Q}$, where $\mathbf{Q} = \mathbf{B}, \mathbf{V}$ (Pashmann & Daly 2008). In general, the turbulence-generated coherent structures at scales near the end of the fluid cascade are associated with small-scale gradients, also reflecting the abundance of available turbulent energy there, which can potentially generate various structures, i.e., current sheets.

3. Results

Figure 2 shows MMS observations of a ~ 4 minute interval in the turbulent quasi-parallel MSH. We compare results obtained by single-point and multipoint techniques. The top panel (a) shows the fluctuations of the magnetic field. In

panel (b) the absolute values of the curlometer $|\nabla \times \mathbf{B}|$ (Dunlop et al. 2002) (in black) from the magnetic field are plotted, calculated from the four MMS spacecraft, and resampled to match the ion velocity. Overlaid with green is the smoothed curve at ~ 1.65 s of $|\nabla \times \mathbf{B}|$. We have chosen a smoothing corresponding to the ion inertial length scale (~ 24 km here) because the coherent structures around a current sheet are not fully overlapping, but separated over distances comparable to $\sim d_i$. In our case, the smoothing for the ions is equal to 247 km which for a plasma flow of 150 km s^{-1} corresponds to $\sim 10 d_i$. Such coarse graining by smoothing is done to reach better correlations between currents and vortices. The red horizontal line marks the threshold equal to 1.2, above which the fluctuations deviate from a Gaussian distribution. Figures 3(a)–(d) represent the probability density function (PDF) distributions of the smoothed ion quantities (red) compared to the respective Gaussian distributions (black). The thresholds are shown as vertical light blue lines and are determined empirically as the value at which the observed PDF develop a power-law tail (linear fit as blue dashed lines) significantly deviating from the Gaussian. In order to check for dependence of the threshold, the analysis was repeated using different values, giving similar results. In Figure 2(c), the PVI from MMS 1 (in black) is plotted, obtained for the time delay $\tau \sim 0.15$ s, which is close to the delay of 0.12 s, corresponding to the separation distance in a spacecraft pair of ~ 18 km for an average bulk flow of $\sim 150 \text{ km s}^{-1}$. The PVI(B) time series of the other spacecraft look very similar because the spacecraft are close to each other. Again, the same smoothing technique is applied and the horizontal red line depicts the threshold of 1.2 (see also Figure 3(a)). The physical meaning of PVI conditioning has been justified in simulations (Greco et al. 2008) and confirmed in observations (Vörös et al. 2016), and enables us to infer the enhanced current densities to non-Gaussian PVI(B). From Figure 2(d), we can see that there is a good correlation (> 0.6) between the PVI(B) and $|\nabla \times \mathbf{B}|$ at the times where both quantities are over the thresholds. We use the Pearson correlation to measure their linear dependence. The correlation coefficient is defined as $cc = \frac{1}{N-1} \sum_{i=1}^N \left(\frac{A - \mu_A}{\sigma_A} \right) \left(\frac{B - \mu_B}{\sigma_B} \right)$, where N is the number of data points, and μ and σ denote the mean and standard deviations of the quantities A and B . The correlation coefficient is calculated with running average in 18.5 s windows with 75% overlapping. The black circles depict the correlation coefficients $cc \geq 0.6$ that come from PVIs and rotations in the magnetic field both being above their determined thresholds, while the gray empty circles come from one or both of the correlating quantities being under the thresholds. These are kept in order to retain a reasonable number of points when calculating the correlations. The same annotation applies for the correlations in panels (h) and (i) and the respective panels in Figure 4. Similarly, Figures 2(e)–(g) show the velocity field, the absolute value of the ion vorticity from four spacecraft, the corresponding PVI(V_i) for MMS 1, and their correlation with the thresholds obtained the same way. The correlation between PVI(V_i) and the vorticity is also evident in the case of the ion velocity during the time intervals where the clusters of peaks in both parameters well exceed the thresholds, namely 1.2 for PVI(V_i) and 1.8 for the vorticity (see Figure 3(c), (d)). The correlation between single-point PVI(V_i) and the magnitude of the multipoint vorticity is an unexpected result, demonstrating that this important quantity associated with the turbulent kinetic

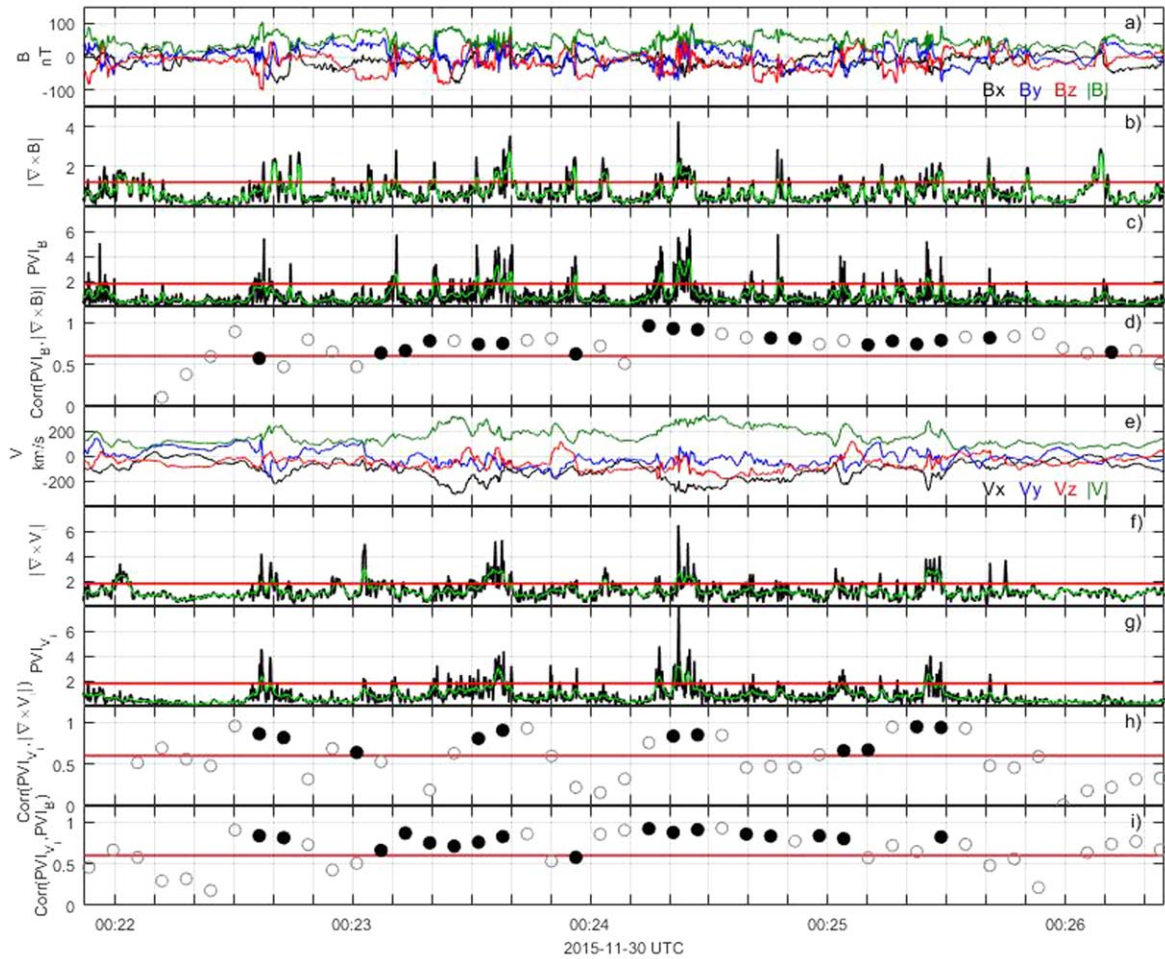


Figure 2. MSH observations by MMS (top to bottom): (a) magnetic field components and magnitude for MMS 1 in the GSE frame; (b) curlometer from the magnetic field from all spacecraft; (c) PVI(B) for MMS 1; (d) correlation between PVI(B) and $|\nabla \times \mathbf{B}|$; (e) ion velocity components and magnitude in the GSE frame for MMS 1; (f) ion vorticity from all spacecraft; (g) PVI(V_i) for MMS 1; (h) correlation between PVI(V_i) and ion vorticity; and (i) correlation between PVI(V_i) and PVI(B). The black circles in the correlation panels mark the correlation coefficients, cc , coming from the quantities above their respective thresholds for $cc \geq 0.6$; the empty gray circles are correlations from noise, i.e., from values under the thresholds. The green curves in (b), (c), (f), and (g) represent the smoothed parameters used in the correlation calculations.

energy of the flow can perhaps be estimated with good approximation using single-point in situ measurements in the solar wind. The last panel (i) of Figure 2 demonstrates the correlations between PVI(V_i) and PVI(B), where we can see that there are blobs of activity in both quantities. This seems to support our working hypothesis that the intermittent excess of the kinetic energy of turbulent plasma manifested by the enhanced vorticity or flow shears is associated with the occurrence of magnetic coherent structures in spatial blobs. Moreover, single-point measurements can be used to find this important correspondence between the ion velocity and magnetic field fluctuations.

Figure 4 follows the logic of Figure 2, presenting the results for the same MSH interval only with the difference that we plot here the quantities related to the electrons—electron velocity V_e (panel (e)), electron vorticity (panel (f)), PVI(V_e) (panel (g)), correlations between PVI(V_e) and electron vorticity (panel (h)), and between PVI(V_e) and PVI(B) (panel (i)). The time delay is 0.12 s corresponding again to the spacecraft separation, and the window length for the correlation averages and the smoothing (in green) is of the order of $\sim 3.5 d_i$, so that we can better see the details in the correlations. The red lines in the panels mark the non-Gaussian thresholds in PVI (panels (c), (g)), and

between B and V shears (panels (b), (f)), as well as correlation thresholds in panels (d), (h), and (i). The parameters based on electron velocity in Figure 4 show characteristics similar to those based on ion velocity in Figure 2, namely, simultaneous deviations from Gaussianity with values 1.3 for $|\nabla \times \mathbf{B}|$, PVI(B) and PVI(V), and 7 for $|\nabla \times \mathbf{V}|$ (Figures 3(e)–(h)). However, due to the higher electrons sampling rate, there are finer details that are well visible in the correlation in Figures 4(h) and (i) and also there are some different features, which will be discussed in the next section.

Next, we present the testing results for the KHI (Figure 5). In general, KH vortices are large-scale structures reaching the size of several R_E at the flank of the magnetosphere. In the considered event of 2015 September 8, 10:07–11:25 UTC, the average size of the vortices was $\sim 2.8 R_E$. The MMS spacecraft were positioned at $\sim (4.9, 9.1, \text{ and } 0.1) R_E$ in the GSE frame, at a separation of ~ 175 km, which in the time domain corresponds to 0.6 s for average plasma bulk 275 km s^{-1} . The entire interval is about 2 hr long. For the sake of better visualization of the details, a 5 minute long time interval is shown in the figure. The KH vortices can be easily identified as the alternation of all parameters as the MMS spacecraft cross in succession the different plasma regions. From previous Cluster

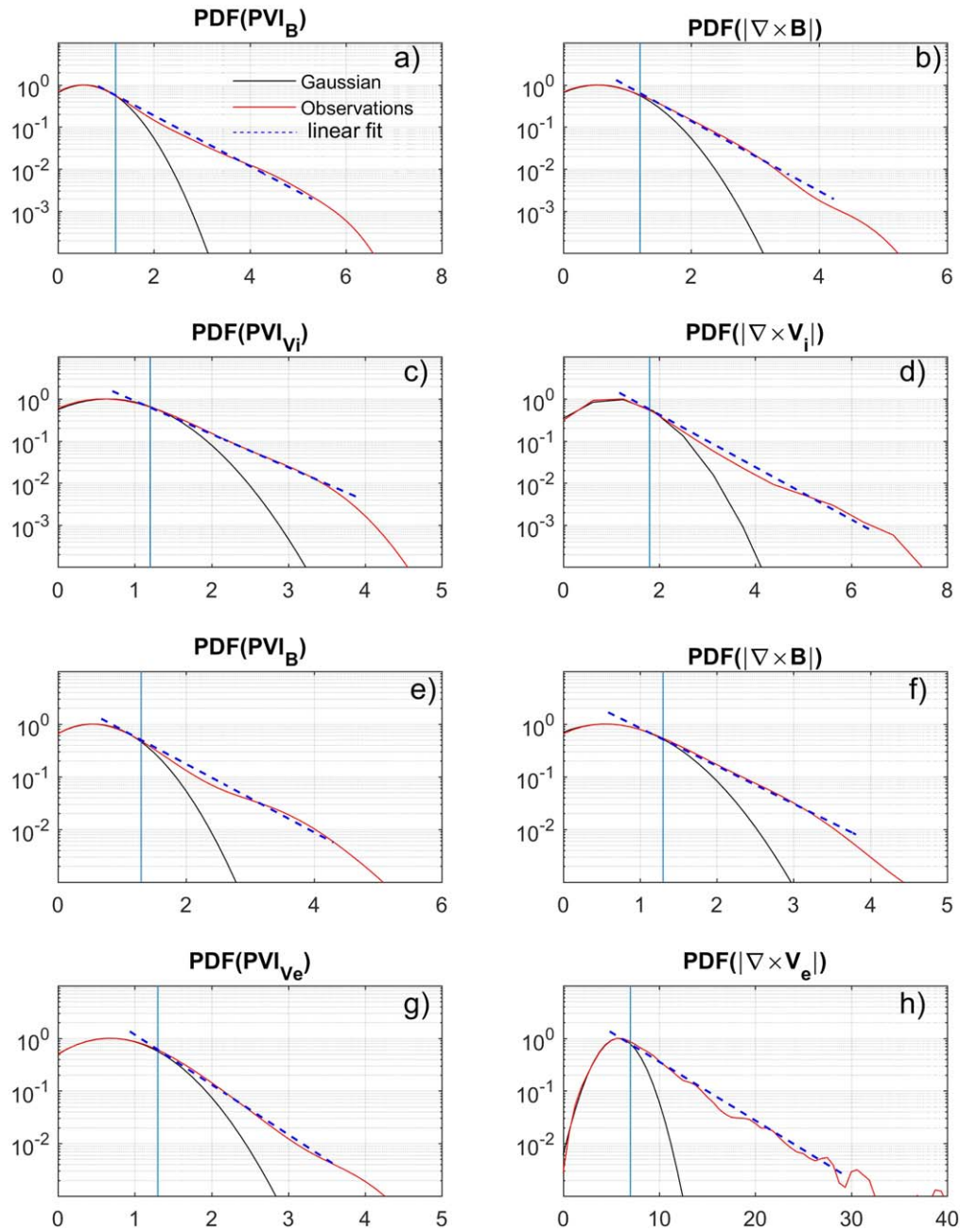


Figure 3. PDFs (in red) of the smoothed $PVI(B)$, $PVI(V)$, $|\nabla \times \mathbf{B}|$ in units [mA m^{-2}], and $|\nabla \times \mathbf{V}|$ in [1 s^{-1}]. In black are shown the respective Gaussian distributions. The vertical light blue lines mark the thresholds where the deviations from the Gaussian are observed. Above these thresholds the long PDF tails can be fitted linearly (blue dashed lines). Panels (a)–(d) ((e)–(h)) represent the quantities related to ion (electron) observations. The respective smoothing procedure is described in the text.

observations with larger spacecraft separations (thousands of kilometers) (Hasegawa et al. 2004), it was shown that due to the relative plasma motion between the fast MSH flow at the flanks of the magnetopause and the stagnant magnetospheric low latitude boundary layer (LLBL) plasma, KHI can grow. When KHI has grown sufficiently the high-density plasma from MSH and the low density LLBL plasma on both sides of the magnetopause get engulfed and en-rolled into vortices bearing the characteristics of the two plasma regions. If we focus on the interval 11:02:00–11:02:50, the part that belongs to the MSH plasma is characterized by a stronger magnetic field (panel (a)), higher ion velocity (panel (e)), and lower ion and electron temperatures (panels (i), (j)), while the part dominated by the

LLBL has reverse features—lower magnetic field and velocity, and higher temperature. Another characteristic feature is the presence of periodic current sheets formed in the process of the vortex en-rolling (in color shades). For example, the current sheets at $\sim 11:01:20$ and $\sim 11:02:50$ are detected by both single and multi-spacecraft techniques: strong peaks in the $PVI(B)$ (panel (b)), where the gray curve is the single-point measurement and the black—the two-point one; together with the magnetic field shear angle (Equations (3) and (4)) (panel (c), same color nomenclature) coming from the sharp changes in the magnetic field direction (panel (a)) observed by MMS 4, which are also detected at the same times with the spacecraft tetrahedron and appear as large peaks in the component of

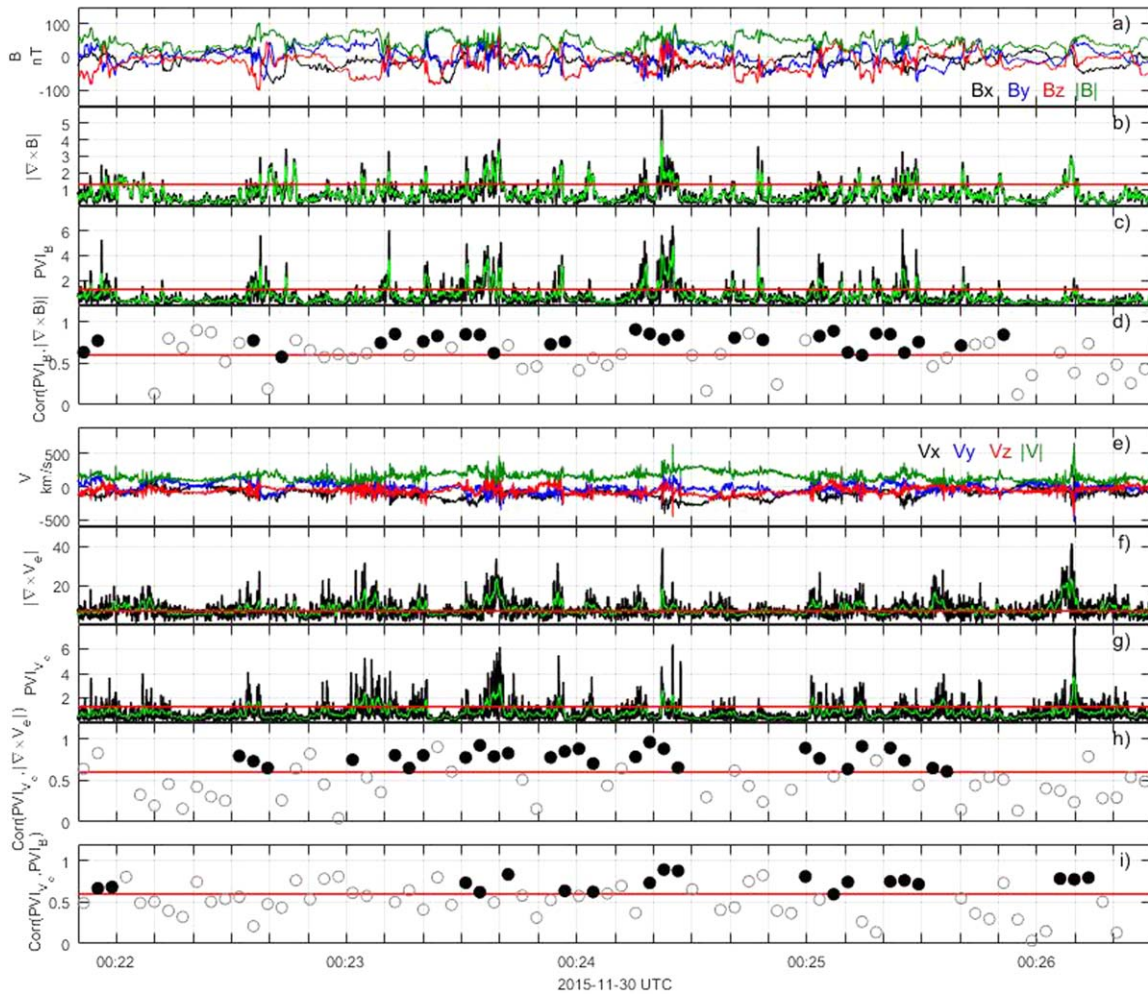


Figure 4. MSH observation by MMS (top to bottom): (a) magnetic field components and magnitude in the GSE frame; (b) curlometer from the magnetic field from all spacecraft; (c) $PVI(B)$ for MMS 1; (d) correlation between $PVI(B)$ and $|\nabla \times \mathbf{B}|$; (e) electron velocity components and magnitude for MMS 1 in the GSE frame; (f) electron vorticity from all spacecraft; (g) $PVI(V_e)$ for MMS 1; (h) correlation between $PVI(V_e)$ and electron vorticity; and (i) correlation between $PVI(V_e)$ and $PVI(B)$. The colored circles in the correlation panels mark the correlation coefficients, cc , coming from the quantities above their respective thresholds for $cc \geq 0.6$; the empty gray circles are correlations from noise, i.e., from values under the thresholds. The green curves in (b), (c), (f), and (g) represent the smoothed parameters used in the correlation calculations.

$|\nabla \times \mathbf{B}|$ along Z , which is the direction of vortex in-rolling (panel (d)). We have also calculated the single-point and two-point $PVI(V_i)$ (panel (f)), ion velocity shear angle (Equations (3) and (4)) (panel (h), in gray and black, respectively), and the three components of the four-point ion vorticity (panel (h)). The vortices' detection can be easily seen by following the flow rotation and velocity gradients in these panels. Characteristic of the KHI is also that the temperatures are periodically changing because of plasma mixing (panels (i), (j)). To see if there are local peaks in the temperature that are not intrinsic to the different regions but might be associated with enhanced $PVI(B)$ and $PVI(V)$, rotation angles, and vorticity, we filter out the large-scale variation in the ion temperature due to different regions crossings (red curve in panel (i)). We applied the same technique for the electron temperature but the structures were not very well seen. Indeed, the filtered T_e reveals local peaks that seem to occur in the intervals of the current sheets (in color shading).

In Figure 6 we exemplify this by zooming in into the orange shaded interval. Outside the shaded box, the plasma velocity and the magnetic field are very quiet and the ion temperature is steady and non-fluctuating. Inside the

highlighted interval, however, there is enhanced activity—at the times of the peaks in $PVI(B)$ and magnetic field rotation (panels (b)–(d)), there are also strong velocity shears and vorticity (panels (f)–(h)). Remarkably, the local increases in the ion temperature correlated quite precisely with the increases in the discussed parameters, which strongly suggests that the observed ion heating is associated with the currents sheets generated by the enhanced vorticity.

Finally, we investigate an interval from an ICME event observed by WIND at L1 (Figure 7). In this figure, we plot only the ICME sheath, which is the region confined between the IP shock (magenta vertical line) at 05:23 UTC on 2013 March 17 and the leading edge of the magnetic cloud at $\sim 14:35$ UTC (defined by the temperature and plasma beta drop and the lack of strong fluctuations in all variables) on the same day. The preceding solar wind and the part of the magnetic cloud are shaded in gray and beige, respectively. The ICME was fast with shock speed 650 km s^{-1} and an average sheath speed 700 km s^{-1} . The shock Mach number $M_A = 6.1$ and the magnetosonic number $M_S = 4.2$, according to the *IPshocks* database (<http://ipshocks.fi/>). The downstream geometry is quasi-parallel with an angle between the shock normal and the

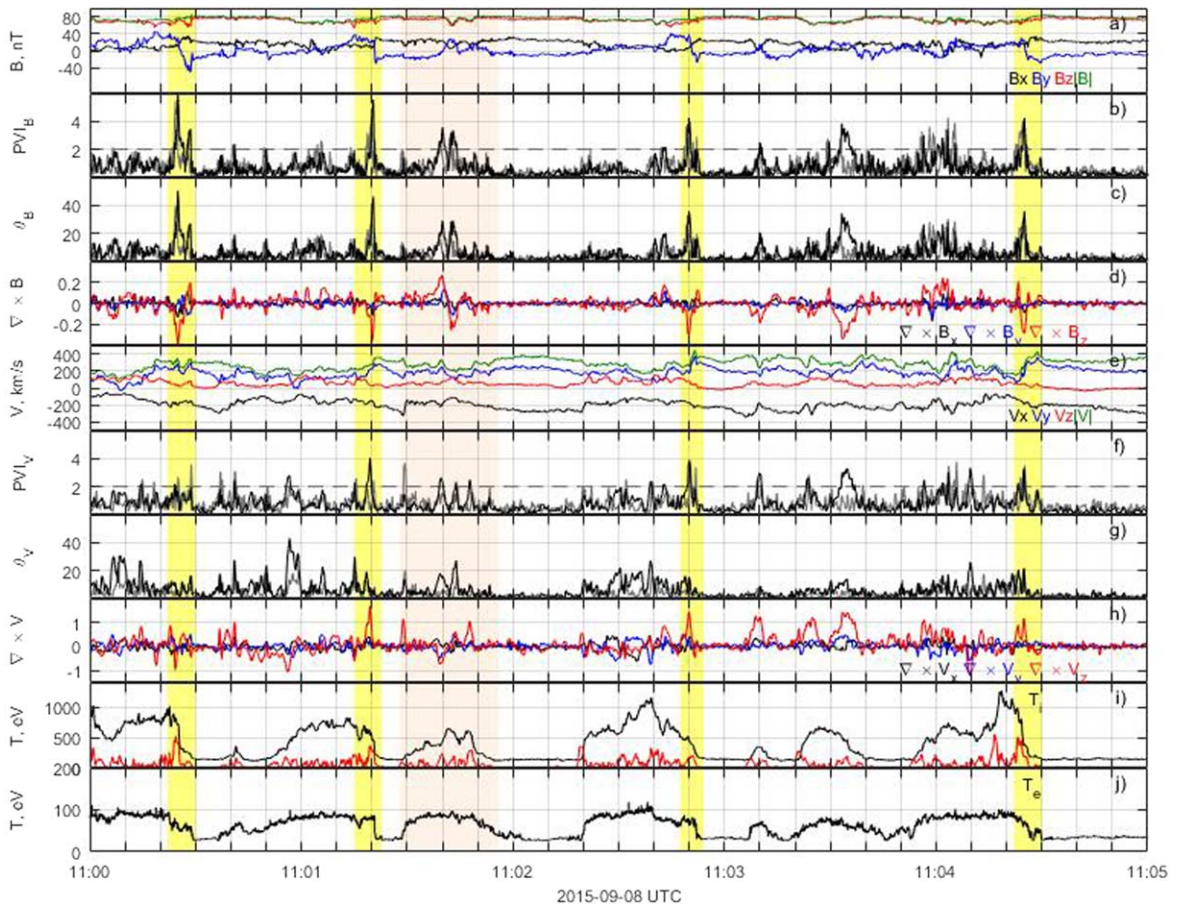


Figure 5. MMS observation of KH vortices (top to bottom): (a) magnetic field magnitude and components for MMS 4; (b) single-point $PVI(B)$ (gray) from MMS 4 and two-point $PVI(B)$ calculated for the MMS 2 and MMS 4 pair of spacecraft with time shift $\tau = 0.6$ corresponding to the spacecraft separation; (c) magnetic shear angle from MMS 4 (gray), and from MMS 2 and MMS 4 (black); (d) $|\nabla \times \mathbf{B}|$ components from all spacecraft; (e) velocity magnitude and components for MMS 4; (f) $PVI(V)$ for MMS 2–4 (black) overlaid on $PVI(V)$ for MMS 4; (g) velocity shear angle for MMS 4 (gray), and the pair MMS 2 and MMS 4 (black); (h) ion vorticity components from all spacecraft; (i) ion temperature—measured (black) and filtered (red) for MMS 4; and (j) electron temperature for MMS 4. The horizontal dashed gray lines mark the PVI threshold. The shaded intervals highlighting current sheets are discussed in detail in the text.

upstream magnetic field direction $\theta_{B_n} \sim 35^\circ$. Overall, the entire sheath region is highly variable, with large fluctuations in the magnetic field often changing sign compared to the preceding solar wind (Figure 7(a)). This is especially true in the part close to the IP shock, where there is also plasma compression (panel (i)), strong plasma heating (panel (h)), and high ion plasma beta (panel (j)). Similarly to the MSH cases, we calculate $PVI(B)$ and $PVI(V)$ of the ion bulk velocity, and magnetic and velocity shear angles from single-point measurements using a time shift $\tau = 30$ s (in black) in panels (b), (c), (e), and (f), respectively. The timescale is chosen to be as close as possible to the kinetic range and not to affect the accuracy of the PVI estimation by an insufficient number of points due to the low sampling frequency of the plasma data. To verify that the structures are current sheets ($PVI > 3$) we also plot in gray the PVIs and shears from the smallest accessible scale $\tau = 6$ s. The magnetic field makes several rotations from 0° – 180° behind the IP shock until 07:50 UTC (panel (b)). Some of these rotations are associated with high $PVI(B)$ peaks (panel (c)), confirming the presence of current sheets. At the same time, there are no sharp gradients and rotations in the velocity field (panels (d), (f)) in this interval, except for the $PVI(V)$ peak accounting for the detection of the shock (panel (e), the threshold is denoted by the dashed green line). Looking deeper inside the sheath there are periods of smooth magnetic field with no directional

changes and shears adjacent to shorter periods (highlighted in yellow) characterized by peaks in both $PVI(B)$ and $PVI(V)$ (panels (b), (e)), and strong magnetic shears (panel (c)). Although much smaller than the magnetic field ones, the velocity shears are significant relative to the quiet intervals with a smoother magnetic field, velocity, and temperature in between the yellow shaded boxes. Panel (g) shows the correlation coefficient between $PVI(B)$ and $PVI(V)$ (red line with circles), obtained from running averages with 50% overlapping windows of ~ 260 points. The correlation coefficients are calculated as the average in scales ranging from 6–120 s (gray dashed lines), which fall into the higher frequency part of the MHD range close to the beginning of the kinetic range. Notably, there is a very strong correlation between $PVI(B)$ and $PVI(V)$ in the active regions (the horizontal green line marks the 0.6 threshold), which coincides with temperature enhancements. Interestingly, the plasma beta (panel (j)) is also nearly constant in the interval 07:50–13:30 UTC comprising these active and quiet regions.

4. Discussion

The MSH interval studied here is relatively short (4 minutes long); however, it represents well-calibrated data. The MSH geometry is quasi-parallel with several current sheets detected.

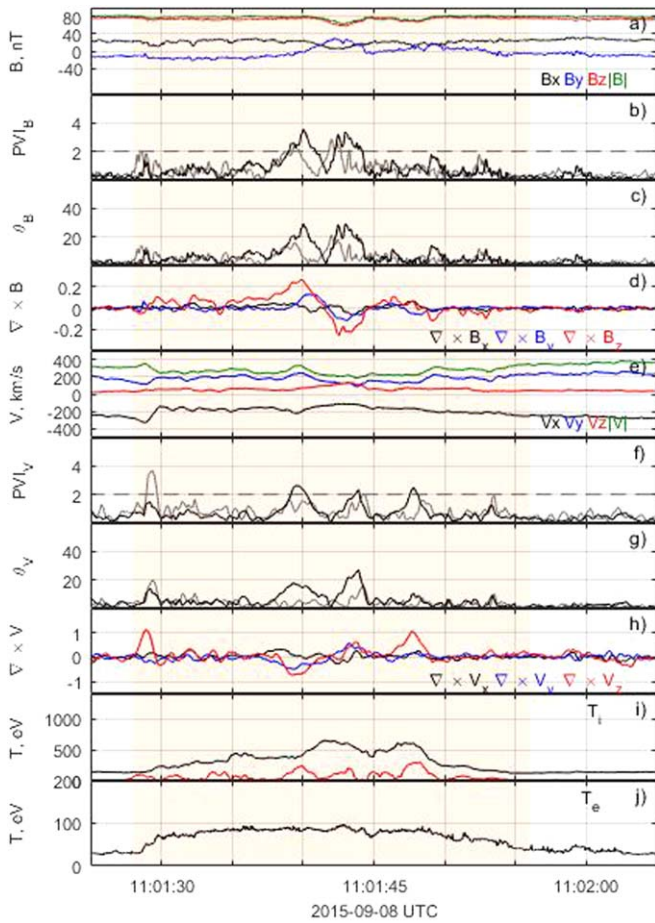


Figure 6. The interval 11:01:28–11:01:56 from Figure 5 zoomed in to highlight in the shaded area—the enhanced ion temperature (in red, panel (i)), associated with a group of current sheets (panels (b)–(d)) and large $PVI(V_i)$, velocity shear, and vorticity components (panels (f)–(g)).

Recently, observations in quasi-parallel MSH have revealed correlations between the electron heating and strong $PVI(B)$ (Chasapis et al. 2015, 2017) at abundant current sheets (Retinò et al. 2007; Vörös et al. 2016; Yordanova et al. 2020). This particular MSH time interval has been the subject of many studies concerning different kinetic processes such as magnetic reconnection in thin current sheets (Yordanova et al. 2016; Vörös et al. 2017), electron acceleration at a current sheet (Eriksson et al. 2016a), whistlers and lower hybrid waves at a reconnection site (Vörös et al. 2019a), energy dissipation (Vörös et al. 2019b), and non-Maxwellian features of the ion VDFs (Perri et al. 2020). This event is ideally suitable to test our hypothesis and methods on the replacement of MMS four-point high-resolution tetrahedron measurements with one-point proxies. The current sheets are represented by the sharp magnetic field gradients and rotations centered roughly, e.g., at 00:22:40, 00:23:10, 00:23:30, 00:24:22, 00:25:03, 00:24:48, 00:25:50, and 00:26:10 UTC, (Figures 2(a), (b), and (c)). The curlometer $|\nabla \times \mathbf{B}|$ (panel (b)) was introduced as a proxy for the current density under the assumptions that the changes in the magnetic field between the spacecraft in the tetrahedron are time independent and linear (Dunlop et al. 2002). The correlation between the single-point $PVI(B)$ and four-point current density from the curlometer techniques has been established earlier in other MSH observations (Chasapis et al. 2017; Yordanova et al. 2020). This is confirmed in our case as

well, where we observe a high correlation between the $PVI(B)$ and $|\nabla \times \mathbf{B}|$ (panel (d)).

The current sheet intervals coincide with large fluctuations and changes in the orientation of the plasma flow (panel (e)). For example, in the interval containing the current sheet at 00:24:22, Eriksson et al. (2016a, see their Figure 1), have identified several jets using the criterion for detecting high pressure flows introduced by Plaschke et al. (2013). This current sheet, seen as the strongest rotation in Figure 2(b) and strong peaks in $PVI(B)$ (panel (c)) is inside one of the jets. This jet can be recognized as the largest vorticity and $PVI(V_i)$ as well (panels (f), (g)). The correlation between the vorticity and $PVI(V_i)$ results from the burstiness of activity in both quantities (panel (h)). Given that the correspondence between one-point and four-point techniques (panels (d), (h)) shows good agreement in the detection of intermittent structures, we now correlate directly the PVI of the magnetic field and the ion velocity (panel (i)). The results show that the correlation is very high in the intervals containing the currents sheets accompanied at the same time with strong shear flows, in analogy with the prediction from numerical simulations (Karimabadi et al. 2013).

Figure 4 represents the same quantities except that now the vorticity (panel (f)) and $PVI(V_e)$ (panel (g)) are calculated from the electron speed (panel (e)). Thanks to the higher sampling rate we can see now more details in the single-point $PVI(V_e)$. In the beginning of the interval there are correlations (panels (d), (h), (i)) detected by the one-point parameters coming from smaller-scale magnetic field and velocity gradients (panels (c), (g)), which were not visible in the ion data (Figure 2). The same is true for the current sheet at 00:26:10, where correlations can only be seen in the electron data from the single-point PVI s (Figure 4(i)). This current sheet has been associated with signatures of a reconnection (Yordanova et al. 2016), where no clear ion outflow but only electron jets have been found. There also occurs the strongest fluctuation in the velocity (Figure 4(a)) and it is represented by the largest velocity gradient and shear (panels (f), (g)). There is also a reverse case for the structure at 00:22:30–00:22:40 UTC, where there is no single-point $PVI(B, V_e)$ correlation in the electron data (panel (i)), but there is a correlation in the ion data (Figure 2(i)). This indicates that the velocity and magnetic field gradients are possibly generated over larger ion scales. At this point, it is worth emphasizing the importance of the PVI conditioning in distinguishing the coherent structures from the noise. One should also consider whether the measurement resolution can resolve the scales, which are under investigation, as well as to keep in mind in the case of multipoint measurement that the PVI detection would be limited to structures that are larger than the corresponding spatial separation of the spacecraft. Apart from the above-mentioned examples, the intervals with correlations characterizing the rest of the regions of the currents sheet coincide with electron and ion data. This reflects the multi-scale nature of the intermittent coherent structures, in analogy to observations in the turbulent solar wind (Greco et al. 2016), and that the current sheets are associated with regions of strong vortical flows (Karimabadi et al. 2013). Vorticity and flow shears do not affect only the plasma dynamics but can lead to additional instabilities driven by shear-induced pressure anisotropy. A non-gyrotropic electron pressure tensor then represents the dominant non-ideal

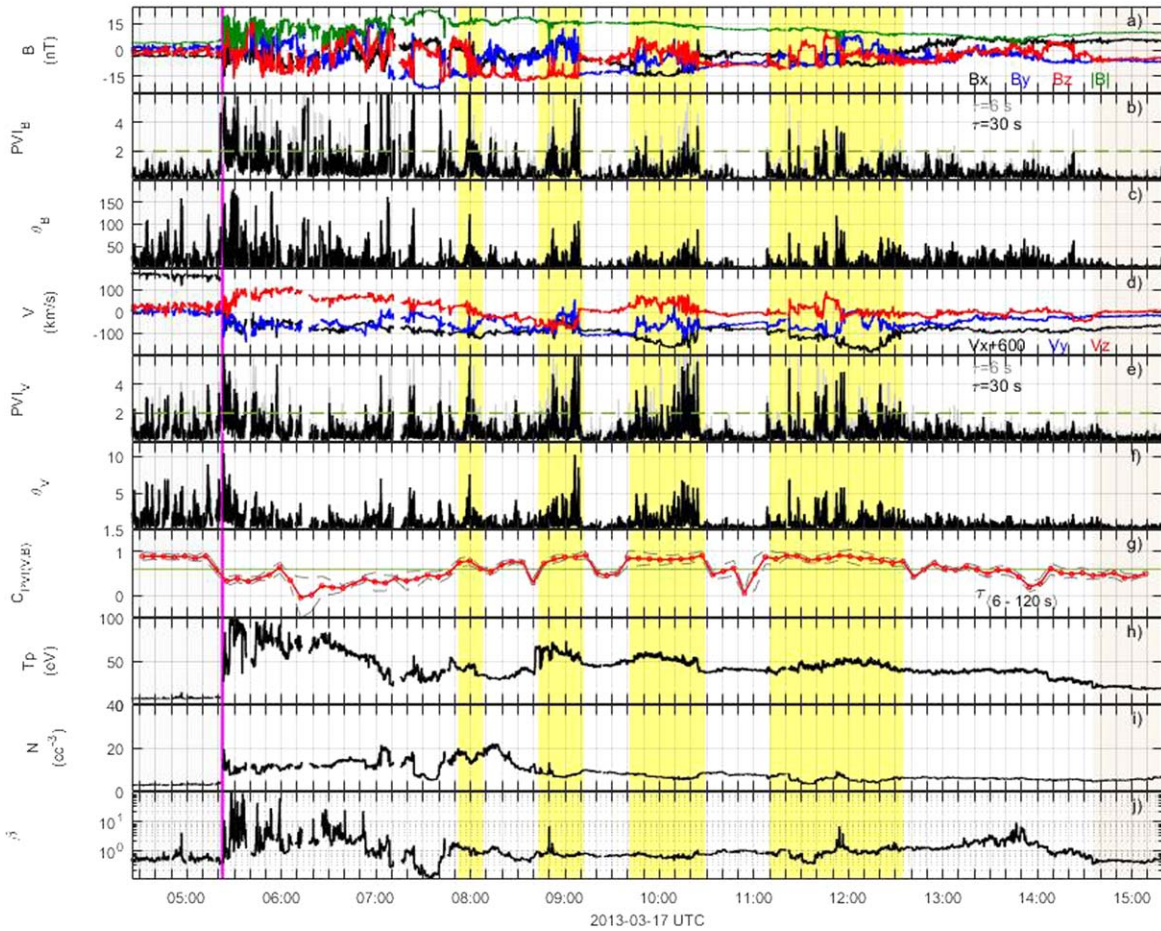


Figure 7. CME sheath observation by WIND spacecraft bounded by the gray shaded box marking the preceding solar wind and the beige box, marking the boundary layer at the magnetic cloud’s leading edge. The vertical magenta line represents the associated IP shock. The yellow boxes highlight the intervals with intermittent plasma heating. (a) magnetic field components and intensity in GSE; (b) PVI(B) for time delays $\tau = 30$ s (in black) and $\tau = 6$ s (in gray); (c) magnetic field rotation for the same time delay for the same delays; (d) ion bulk velocity (V_z component shifted with 600 km s^{-1}); (e) PVI(V), (f) velocity shear angle for the same τ values; (g) correlation between PVI(B) and PVI(V), where the green horizontal line marks the threshold 0.6, the red dashed curve is the average correlation obtained for the range of time delays from 6–120 s (dashed gray curves); (h) proton temperature; (i) proton density; and (j) proton plasma beta.

term in generalized Ohm’s law driving magnetic reconnection (Del Sarto et al. 2016).

We continue to further discuss the application of the proposed method to the large KH vortices. The consecutive changes from high to low temperatures in Figures 5(i) and (j), are due to the spacecraft passing through different plasmas of LLBL and MSH origin. It is difficult to observe local peaks in the ion and electron temperature that are not associated with different regions themselves; however, near the LLBL boundaries, there are additional temperature elevations in the vicinity of the current sheets. These local enhancements in T_i associated with the proxies and the curlometer and vorticity could be made visible when the large-scale variations were removed (red curve in panel (i)). Similarly, in Osman et al. (2012) and Sorriso-Valvo et al. (2018) it was shown, that in order to identify correlations between turbulent structures and local heating a conditional average analysis is needed to allow the persistent but weak heating to emerge from the turbulent temperature fluctuations.

Inside the current sheet at 11:02 UTC (yellow shaded), characterized by peaks in the PVI(B) (panel (b)) and magnetic shear (panels (c), (d)), there is a plasma jet discerned by strong vorticity and large PVI(V_i) in (panels (g), (h)). At the same interval, both ion and electron temperatures are elevated. This

jet was recognized previously as a result of magnetic reconnection (Eriksson et al. 2016b), where also two of the MMS spacecraft crossed the electron diffusion region and observed significant electron parallel heating (Eriksson et al. 2016c). One can see similar features of enhanced ion and electron temperature, and high gradients and vorticity in other current sheets (yellow shaded). In fact, this more than 2 hr KH event has been recognized as the first observation of reconnection exhausts occurring in more than half of the cases of the current sheets associated with the KH waves (Eriksson et al. 2016b). Therefore, we can directly relate some of the observed plasma heating with the energy dissipation due to magnetic reconnection.

With the events of MSH turbulence and large KH vortices at the magnetospheric flanks, we have shown that single-point PVIs represent well the detected gradients and shears by the multi-spacecraft proxies. While in the MSH turbulence there can be more than one competing kinetic process responsible for the energy conversion that can be accounted for by the plasma heating (Vörös et al. 2019b), in the KH vortices with this method we could connect individual current sheets with plasma heating.

Despite the recent advances in the collisionless plasma heating problem (Tong et al. 2019; Halekas et al. 2020;

López et al. 2020; Zhao et al. 2020), it is still unclear how heating is generated in larger plasma volumes with numerous intermittent current sheets and shear flows. Although the comprehension of individual heating events is crucial, the volume integrated heating, even if it involves specific field and plasma structures only, might offer a further understanding of energy conversions in real large-scale systems such as the solar corona or the solar wind. For this purpose, we apply the method to the turbulent ICME sheath, which is part of a large IP transient. It is very clear from Figure 7, that ~ 2 hr downstream of the IP shock (magenta vertical line), the temperature enhancements occur intermittently in blobs of a duration of tens of minutes (in yellow) corresponding to the range of 135–580 ion inertial lengths. In terms of the introduced proxies, these blobs contain the current sheets (enhanced PVI(B) and rotation angle), the vortical sheared flows (enhanced PVI(V) and rotation angle), and correlations between them that are over the threshold. In other words, we refer to such blobs as groups of current sheets associated with vortices and high plasma temperature. Obviously, the heating mechanisms in the vicinity of the IP shock manifested in low correlations between PVI(V) and PVI(B) (panel (j)) but high T_i (panel (h)) are different. We can also speculate that the proposed method works rather well in this event because of the non-fluctuating low-beta plasma. In ICME sheaths with strongly fluctuating plasma beta, it would be more difficult to observe the outlined correlations. Investigations into this direction are postponed to further studies.





5. Conclusions

In this paper, we introduced a new pathway for plasma heating in intermittent blobs not considered before in space plasma experiments. Although there is no exact theory for coherent structure formation near ion scales, there exist simulation and experimental results that turbulence can generate such structures. Since the blobs are much larger than the ion inertial length ($100 R_E$ or larger) the turbulent processes generating these intermittent structures are of fluid scale. The one-point proxies replacing the four-point $|\nabla \times \mathbf{B}| (=j)$ and $|\nabla \times \mathbf{V}|$ (vorticity) are introduced from necessity to better understand turbulent heating in the solar wind. Because of the above reasons, the proxies are not based on rigorous mathematical relations but represent approximations and generalizations corresponding to previous simulation and experimental results. The proxies seemed to be useful in describing heating in larger blobs in the sheath region of an ICME, where plasma beta was low without strong fluctuations. It is known from previous studies (Phan et al. 2010) that when plasma beta is changing strongly across a reconnecting current sheet, reconnection is stopped or the current sheet is destroyed. This suggests that further statistical studies based on the proposed proxies will be needed to investigate the parameter space validating this approach under different conditions. It is also a challenge for further analysis to identify the turbulent multi-scale structures that are responsible for the generation or absence of blobs.

E.Y., L.S.V., and A.P.D. have been supported by Swedish Contingencies Agency, grant 2016–2102. A.P.D. received financial support from the Swedish National Space Agency (Grant 2020-00111). E.Y. and L.S.V. have received financial support from the Swedish National Space Agency

(Grant 145/18). Z.V. has been supported by the Austrian FWF under contract P28764-N27. E.K. acknowledges the ERC under the European Union’s Horizon 2020 Research and Innovation Programme Project 724391 (SolMAG), Academy of Finland Project 310445 (SMASH). European Union’s Horizon 2020 research and innovation program under grant agreement No. 101004159 (SERPENTINE). E.K.’s contribution has been achieved under the framework of the Finnish Centre of Excellence in Research of Sustainable Space (FORESAIL; Academy of Finland grant No. 312390), which she gratefully acknowledges.

ORCID iDs

Emiliya Yordanova  <https://orcid.org/0000-0002-9707-3147>
 Zoltán Vörös  <https://orcid.org/0000-0001-7597-238X>
 Luca Sorriso-Valvo  <https://orcid.org/0000-0002-5981-7758>
 Andrew P. Dimmock  <https://orcid.org/0000-0003-1589-6711>

References

- Adhikari, L., Khabarova, O., Zank, G. P., & Zhao, L.-L. 2019, *ApJ*, **873**, 72
 Adhikari, L., Zank, G. P., Zhao, L.-L., et al. 2020, *ApJS*, **246**, 38
 Burch, J. L., Torbert, R. B., Phan, T. D., et al. 2016, *Sci*, **352**, aaf2939
 Chandran, B. D. G., Li, B., Rogers, B., Quataert, H. E., & Germaschewski, K. 2010, *ApJ*, **720**, 548
 Chasapis, A., Matthaeus, W. H., Parashar, T. N., et al. 2017, *ApJ*, **836**, 247
 Chasapis, A., Matthaeus, W. H., Parashar, T. N., et al. 2018a, *ApJL*, **856**, L19
 Chasapis, A., Retinó, A., Sahraoui, F., et al. 2015, *ApJL*, **804**, L1
 Chasapis, A., Yang, Y., Matthaeus, W. H., et al. 2018b, *ApJ*, **862**, 32
 Chen, C. H. K., Klein, K. G., & Howes, G. G. 2019, *NatCo*, **10**, 740
 Del Sarto, D., Pegoraro, F., & Califano, F. 2016, *PhRvE*, **93**, 053203
 Dunlop, M. W., Balogh, A., Glassmeier, K. H., & Robert, P. 2002, *JGRA*, **107**, A11
 Echim, M. M., Chang, T., Kovacs, P., et al. 2021, in *Magnetospheres in the Solar System*, ed. R. Maggiolo et al. (New York: Wiley), 67
 Eriksson, E., Vaivads, A., Graham, D. B., et al. 2016a, *JGRA*, **121**, 9608
 Eriksson, S., Lavraud, B., Wilder, F. D., et al. 2016b, *GeoRL*, **43**, 5606
 Eriksson, S., Wilder, F. D., Ergun, R. E., et al. 2016c, *PhRvL*, **117**, 015001
 Escoubet, C. P., Fehringer, M., & Goldstein, M. 2001, *AnGeo*, **19**, 1197
 Gary, S. P. 2015, *RSPTA*, **373**, 20140149
 Greco, A., Chuychai, P., Matthaeus, W. H., Servidio, S., & Dimitruk, P. 2008, *GeoRL*, **35**, L19111
 Greco, A., Matthaeus, W. H., Perri, S., et al. 2018, *SSRv*, **214**, 1
 Greco, A., Matthaeus, W. H., Servidio, S., Chuychai, P., & Dimitruk, P. 2009, *ApJL*, **691**, L111
 Greco, A., Perri, S., Servidio, S., Yordanova, E., & Veltri, P. 2016, *ApJL*, **23**, L39
 Halekas, J. S., Whittlesey, P., Larson, D. E., et al. 2020, *ApJSS*, **246**, 22
 Hasegawa, H., Fujimoto, M., Phan, T.-D., et al. 2004, *Natur*, **430**, 755
 Hesse, M., Birn, J., & Kuznetsova, M. 2001, *JGR*, **106**, 3721
 Jain, N., Büchner, J., & Muñoz, P. A. 2017, *PhPI*, **24**, 032303
 Karimabadi, H., Roytershteyn, V., Wan, M., et al. 2013, *PhPI*, **20**, 012303
 Kilpua, E., Good, S., Ala-Lahti, M. M., et al. 2021, *FrASS*, **7**, 109
 Kilpua, E., Koskinen, H. E. J., & Pulkkinen, T. I. 2017, *LRSP*, **14**, 5
 Kilpua, E. K. J., Fontaine, D., Good, S. W., et al. 2020, *AnGeo*, **38**, 999
 Kilpua, E. K. J., Fontaine, D., Moissard, C., et al. 2019, *SpWea*, **17**, 1257
 Lepping, R. P., Acuña, M. H., Burlaga, L. F., et al. 1995, *SSRv*, **71**, 207
 Lin, R. P., Anderson, K. A., Ashford, S., et al. 1995, *SSRv*, **71**, 125
 López, R. A., Lazar, M., Shaaban, S. M., Poedts, S., & Moya, P. S. 2020, *ApJL*, **900**, L25
 Matthaeus, W. H. 2021, *PhPI*, **28**, 032306
 Matthaeus, W. H., Wan, M., Servidio, S., et al. 2015, *RSPTA*, **373**, 20140154
 Matthaeus, W. H., Yang, Y., Wan, M., Parashar, T. N., & Bandyopadhyay, R. 2020, *ApJ*, **891**, 101
 Osman, K. T., Matthaeus, W. H., Wan, M., & Rappazzo, A. F. 2012, *PhRvL*, **108**, 261102
 Pashmann, G., & Daly, P. W. 2008, *Multi-Spacecraft Analysis Methods Revisited* (Noordwijk: ESA Communications)
 Perri, S., Perrone, D., Yordanova, E., et al. 2020, *JPIPh*, **86**, 905860108
 Pezzi, O., Servidio, S., Perrone, D., et al. 2018, *PhPI*, **25**, 060704

- Phan, T. D., Eastwood, J. P., Shay, M. A., et al. 2018, *Natur*, **57**, 202
- Phan, T. D., Gosling, J. T., Paschmann, G., et al. 2010, *ApJL*, **719**, L199
- Phan, T. D., Paschmann, G., Twitty, C., et al. 2007, *GeoRL*, **34**, L14104
- Plaschke, F., Hietala, H., & Angelopoulos, V. 2013, *AnGeo*, **31**, 1877
- Pollock, C., Moore, T., Jacques, A., et al. 2016, *SSRv*, **199**, 331
- Quijia, P., Fratemale, F., Stawarz, J. E., et al. 2021, *MNRAS*, **503**, 4815
- Retinò, A., Sundkvist, D., Vaivads, A., et al. 2007, *NatPh*, **3**, 236
- Russell, C. T., Anderson, B. J., Baumjohann, W., et al. 2014, *SSRv*, **199**, 189
- Servidio, S., Greco, A., Matthaeus, W. H., Osman, K. T., & Dmitruk, P. J. 2011, *JGRA*, **116**, A09102
- Siscoe, G., & Odstrcil, D. 2008, *JGRA*, **113**, A00B07
- Sorriso-Valvo, L., Carbone, F., Perri, S., et al. 2018, *SoPh*, **293**, 10
- Sorriso-Valvo, L., Catapano, F., Retinò, A., et al. 2019, *PhRvL*, **122**, 035102
- Stawarz, J. E., Eriksson, S., Wilder, F. D., et al. 2016, *JGRA*, **121**, 11021
- Sundkvist, D., Retinò, A., Vaivads, A., & Bale, S. D. 2007, *PhRvL*, **99**, 025004
- Taylor, G. I. 1938, *RSPSA*, **164**, 476
- Tong, Y., Vasko, I. Y., Pulupa, M., et al. 2019, *ApJL*, **870**, L6
- Valentini, F., Perrone, D., Stabile, S., et al. 2016, *NJPh*, **18**, 125001
- Vörös, Z., Yordanova, E., Echim, M. M., Consolini, G., & Narita, Y. 2016, *ApJL*, **819**, L15
- Vörös, Z., Yordanova, E., Graham, D. B., Khotyaintsev, Y. V., & Narita, Y. 2019a, *JGRA*, **124**, 8551
- Vörös, Z., Yordanova, E., Khotyaintsev, Y. V., Varsani, A., & Narita, Y. 2019b, *FrASS*, **6**, 60
- Vörös, Z., Yordanova, E., Varsani, A., et al. 2017, *JGRA*, **122**, 11442
- Wu, C.-C., Liou, K., Vourlidas, A., et al. 2016, *JGRA*, **121**, 56
- Yang, Y., Matthaeus, W. H., Parashar, T. N., et al. 2017, *PhPI*, **24**, 072306
- Yang, Y., Wan, M., Matthaeus, W. H., et al. 2019, *MNRAS*, **482**, 4933
- Yordanova, E., Vörös, Z., Raptis, S., & Karlsson, T. 2020, *FrASS*, **7**, 2
- Yordanova, E., Vörös, Z., Varsani, A., et al. 2016, *GeoRL*, **43**, 5969
- Zank, G. P., Adhikari, L., Hunana, P., et al. 2017, *ApJ*, **835**, 147
- Zhao, G. Q., Lin, Y., Wang, X. Y., et al. 2020, *GeoRL*, **47**, e2020GL089720
- Zhao, L.-L., Zank, G. P., Adhikari, L., et al. 2020, *ApJS*, **246**, 26
- Zhao, L.-L., Zank, G. P., Hu, Q., et al. 2019, *ApJ*, **886**, 144
- Zhao, L.-L., Zank, G. P., Khabarova, O., et al. 2018, *ApJL*, **864**, L34